



Tuning the active plane and crystallinity of GaN microcrystals for high-performance supercapacitors through potassium nitrate-mediated synthesis

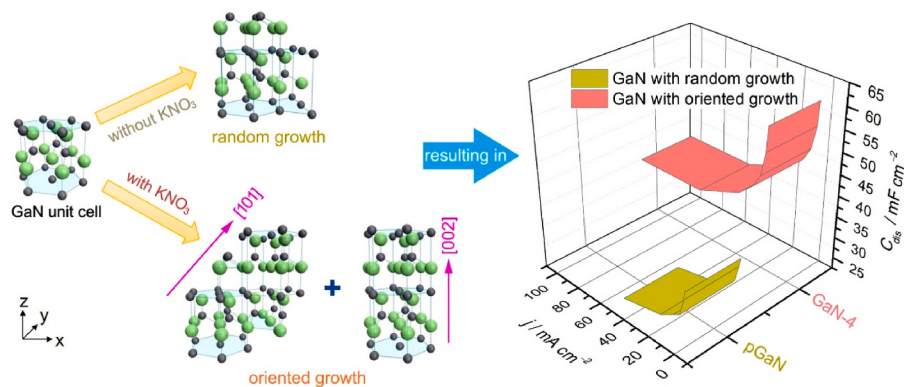
Kai Zhou, Min Zou, Jingwen Guo, Zhen Xu, Wei Hu ^{**}, Yuzhou Zhu, Libin Liu, Ligang Gai ^{*}

Engineering & Technology Center of Electrochemistry, School of Chemistry and Chemical Engineering, Qilu University of Technology (Shandong Academy of Sciences), Jinan, 250353, Shandong, China

HIGHLIGHTS

- The surface atomic structure and crystallinity of GaN microcrystals have been tuned.
- GaN (002) and (101) planes are more active in adsorbing H⁺ compared to (100) plane.
- The energy storage mechanism and electrode kinetics of GaN have been clarified.
- 52 wt% H₃PO₄ is suggested as an electrolyte for powering protonic supercapacitors.
- The GaN-based supercapacitors empowered by 52 wt% H₃PO₄ can operate at -60–60 °C.

GRAPHICAL ABSTRACT



ARTICLE INFO

Keywords:
GaN
Active plane and crystallinity adjustment
Energy storage
Supercapacitor
52 wt% H₃PO₄

ABSTRACT

The surface atomic structure and crystallinity have an important effect on the electrochemical energy storage of electrode materials, in addition to the surface chemistry and textural properties. We report here for the first time that the surface atomic structure and crystallinity of GaN, a renowned electrode material for energy storage, can be tuned by controlling the annealing time via potassium nitrate-mediated synthesis. The underlying mechanism for GaN microcrystals with enhanced intensity ratios of $I_{(002)/(100)}$ and $I_{(101)/(100)}$ manifesting excellent rate performance has been revealed by theoretical computations. The energy storage mechanism and electrode kinetics of the GaN electrodes have been clarified. In addition, the GaN microcrystals-based symmetric supercapacitors empowered by 52 wt% H₃PO₄ can deliver an output voltage of 1.5 V and volumetric specific energy of 11.6 and 40.2 W h L⁻¹ at a specific power of 392.2 W L⁻¹ when operating at -60 and 60 °C, respectively, with electrode material on a commercial loading level.

* Corresponding author.

** Corresponding author.

E-mail addresses: weihu@qlu.edu.cn (W. Hu), liganggai@qlu.edu.cn (L. Gai).

1. Introduction

Metal nitrides (MNs) are being extensively studied as electrode materials for electrochemical energy storage, owing to the advantages in electrical conductivity, corrosion resistance, and electrochemical stability as a result of their unique electronic structure [1–4]. Among the MNs, gallium nitride (GaN) has been considered a promising electrode material for supercapacitors (SCs) due to its high rate capability and cycling stability [5,6]. Similar to the other MNs [7,8], however, the specific capacitance of GaN is insufficient [5], because the M sites manifest a decreased capability to contribute d electrons to adsorbates due to the formation of M–N bonds [9,10].

To improve the specific capacitance of GaN, a simple approach is enlarging the specific surface area by decreasing the grain size to the nanoscale [6,8]. Nonetheless, concerns will be raised on the electrochemical agglomeration of the active materials and side reactions of the electrolytes due to the low thermodynamic stability of nanograins [11]. Also, the low packing density of nanomaterials compromises the volumetric specific capacitance, a key indicator to measure the performance of electrode materials applied in practice [12]. To improve the volumetric specific capacitance, hierarchical structures came to the rescue that are constructed by two or more scales of interconnected and relatively independent structural units [13]. The merits of hierarchical structures integrate the rapid kinetics of nanostructures with the high bulk density of microstructures, providing enhanced rate performance and volumetric specific capacitance for energy storage devices [11]. Therefore, it is of significance to develop GaN electrodes with a hierarchical structure.

On the other hand, the performance of electrode materials is affected by their surface atomic structures. For example, high-index planes of platinum nanocrystals such as (730), (520), and (210) have a high density of atomic steps and unsaturated bonds and exhibit enhanced catalytic activity for anodizing small organic fuels, compared with the most common stable planes such as (100), (111), and (110) [14]. The (100) and (101) planes of metallic Zn with hexagonal structure manifest enhanced surface energy and reduced activation energy of dissolution due to the wavyly arranged plane atoms, compared with the (002) plane in which atoms are arranged in a regular hexagon structure [15]. For hexagonal wurtzite GaN, the (100), (002), and (101) planes are predominant in the XRD spectrum, meaning that atomic arrays that make up the aforementioned planes dominate the surface atomic structure of GaN. However, there has been no report on the influence of the active planes of GaN on interfacial energy storage.

In addition, symmetric SCs empowered by the aqueous electrolyte usually suffer from relatively low specific energy due to the low output voltage limited by the electrochemical stability window (ESW) of water (1.23 V) [5,16,17]. Given the merits of aqueous electrolytes in safety concerns, ionic conductivity, and cost, it is of great significance to improve the specific energy by enlarging the ESW for SCs operating with the aqueous electrolyte. As is documented in the literature [18], the overall conductivity of H_3PO_4 aqueous solution increases with increasing water content and reaches a maximum at a composition of $H_3PO_4 \cdot 5H_2O$. Due to the strong hydrogen bonding between H_3PO_4 and H_2O molecules in $H_3PO_4 \cdot 5H_2O$, the activity of water molecules would be reduced, leading to an enlarged ESW [19]. However, there have been no reports on the performance of SCs operating with $H_3PO_4 \cdot 5H_2O$ electrolyte, in which the weight percent of H_3PO_4 is 52 wt%.

In recent years, there has been increasing interest in developing energy storage devices that manifest impressive performance in extreme environments [20–23], especially in all-temperature environments [24]. However, the employed electrolytes in previous reports are usually made from organic solvents, such as fluorinated carbonate [20], ethyl acetate [21], dimethyl sulfoxide [23], and liquefied gas [24], etc. Reminiscent of the advantages of aqueous electrolytes, it is of high significance to develop energy storage devices that operate with aqueous electrolytes yet manifest superior performance at a wide

temperature range.

In this context, we report for the first time on tuning the active plane and crystallinity of GaN microcrystals for high-performance symmetric SCs by potassium nitrate (KNO_3)-mediated synthesis. The adsorption behaviors of GaN (100), (002), and (101) planes for H_3O^+ and H^+ were clarified by theoretical computations. The operation temperature window of the SCs can be expanded from –60 to 60 °C and the output voltage can be elevated to 1.5 V, using 52 wt% H_3PO_4 aqueous solution as the electrolyte. To satisfy the requirement on electrode loading mass for commercial SC electrodes [25,26], the SC performance was further evaluated by setting the loading mass of GaN at 10 mg cm^{–2} on a single electrode. The GaN-based symmetric SCs can output volumetric specific energy of 11.6 and 40.2 W h L^{–1} at a specific power of 392.2 W L^{–1} when operating at –60 and 60 °C, respectively, showing great potential for application in the environment with significant temperature change.

2. Experimental Section

2.1. Materials

Nominally dry and analytically pure H_3PO_4 (A.R.) was obtained from Aladdin Biochemical Technology Co., LTD (Shanghai, China). Analytically pure KNO_3 , benzene, and melamine were purchased from Sino-pharm Chemical Reagent Co., Ltd (Shanghai, China). Anhydrous $GaCl_3$ was synthesized through a combustion method (equation (1)). The as-obtained $GaCl_3$ was dispersed into anhydrous benzene for use.



2.2. Electrolyte preparation

The electrolyte was prepared by dissolving a certain amount of solid H_3PO_4 into quantitative distilled water. The weight percent of H_3PO_4 in the electrolyte was 52 wt%, conforming to the chemical composition of $H_3PO_4 \cdot 5H_2O$.

2.3. KNO_3 -mediated synthesis of GaN microcrystals

GaN microcrystals were synthesized by a carbothermal reduction method [27]. In brief, 4 mmol melamine, 0.8 mmol KNO_3 , and 3.2 mL of 1 mol L^{–1} $GaCl_3$ were mixed at room temperature and relative humidity of 75–80 %. The molar ratio of KNO_3 to $GaCl_3$ (K/Ga) is 1:4. The resulting uniform precursor was placed into a corundum crucible with a monocrystalline silicon wafer at the bottom. The crucible was placed into a tube furnace, followed by annealing treatment at 800 °C for 4–7 h under a nitrogen atmosphere, with a heating rate of 5 °C min^{–1}. The furnace was allowed to cool to room temperature. The resulting khaki powders were collected, washed thoroughly with distilled water, and finally dried at 80 °C for 6 h. The samples were named GaN-*t*, where *t* denotes the annealing time. In control experiments, the precursor was obtained by mixing melamine with $GaCl_3$ benzene solution without adding KNO_3 , with otherwise identical conditions. The sample derived from annealing the KNO_3 -absent precursor at 800 °C for 6 h was named pristine GaN (pGaN). In addition, the samples derived from annealing the precursors with K/Ga molar ratios of 1:9 and 3:7 at 800 °C for 6 h were named GaN-6-1/9 and GaN-6-3/7.

2.4. Characterization

X-ray diffraction (XRD) spectra were recorded on a Rigaku SmartLab SE automated multipurpose X-ray diffractometer. Scanning electron microscopy (SEM) images were taken by a Hitachi Regulus8220 field emission scanning electron microscope. Raman spectra were collected by a Renishaw inVia laser confocal Raman spectrometer using a 532 nm

excitation wavelength at room temperature. Transmission electron microscopy (TEM) images were taken by a JEOL JEM-2100 high-resolution transmission electron microscope. Measurements by X-ray photoelectron spectroscopy (XPS) were performed on a Thermo Fisher Scientific Escalab 250 X-ray photoelectron spectrometer, using monochromatic Al Ka radiation (1486.6 eV). Gaussian–Lorentzian functions were used to fit the high-resolution XPS spectra calibrated by setting C 1s at 284.8 eV. The specific surface area (S_{BET}) of the samples was measured on a micromeritics ASAP 2460 sorptometer at liquid-nitrogen temperature, using the Brunauer–Emmett–Teller (BET) method. The Barrett–Joyner–Halenda (BJH) method was used to plot the pore size distribution. Before S_{BET} measurements, the samples were degassed at 120 °C for 12 h. Measurements by differential scanning calorimetry (DSC) were conducted by a TA Instruments DSC2500 differential scanning calorimeter. To eliminate the effect of thermal history that results from storage time and temperature [28], sample electrolytes (10–15 mg) were sealed and heated from room temperature to 50 °C, and then cooled to –80 °C. The sample electrolytes were kept at –80 °C for 5 min and then heated to 50 °C, with a ramp rate of 10 °C min^{−1}.

2.5. Theoretical computations

All computations were performed based on density functional theory (DFT) using the Vienna ab initio simulation package (VASP) code and employed the projector augmented wave (PAW) method [29–31]. The exchange-correlation function employs the Perdew–Burke–Ernzerhof (PBE) form of the generalized gradient approximation (GGA) [32]. Optimal structures were achieved using a plane-wave kinetic cutoff of 450 eV and a k -point mesh of $3 \times 3 \times 1$. The optimization process followed the convergence criteria, with electronic and force thresholds set at 10^{−5} eV and 0.02 eV Å^{−1}, respectively. The adsorption energy (E_{ads}) of the adsorbate on the specific GaN surface is defined as $E_{\text{ads}} = E_{\text{total}}(\text{GaN} + \text{adsorbate}) - E(\text{GaN}) - E(\text{adsorbate})$ (equation 2), where E_{total} represents the total energy per supercell for the systems.

The GaN (002) surface was modeled with a (4 × 4) supercell containing a five double atomic layer slab and a minimum 15 Å vacuum region. Similar surface areas were adopted for the GaN (100) and (101) models. For solid-phase simulations, the lowermost three layers were fixed, and the dangling nitrogen and gallium atoms on the bottom surface were passivated with hydrogen saturation. The adsorption structures of H₃O⁺ and H⁺ on the GaN (100), (002), and (101) planes were generated by using the VESTA software [33].

2.6. Electrochemical tests

A coating method was used to prepare the working electrodes, using the stainless-steel mesh as the current collector. To prepare the slurries, the active material, polyvinylidene fluoride, and acetylene black (8:1:1, w/w) were thoroughly mixed in N-methyl pyrrolidone, followed by coating them on the current collector with size of 1 cm × 1 cm. The active material on the working electrodes was 3.5–10 mg cm^{−2}. After being dried in a vacuum oven at 80 °C for 12 h, the working electrodes were subjected to roller pressing to make close contact between the active material and the current collector. In the three-electrode system, the counter electrode is platinum sheet, the reference electrode is Hg/Hg₂SO₄, and the electrolyte is 1 M H₂SO₄. In the two-electrode system, symmetric SCs were constructed in the type of R2032 coin cells in ambient conditions, using 52 wt% H₃PO₄ as the electrolyte and cosmetic special cotton tissue (Poetic Silk, Zhejiang Youquan Electronic Commerce Co., LTD, China) as the separator.

The electrochemical tests of the electrolyte, working electrodes, and SCs were performed on a CHI 760E electrochemical workstation (Shanghai CH Instrument Co., China), including the linear sweep voltammetry (LSV), alternating current (AC) electrochemical impedance spectroscopy (EIS), cyclic voltammograms (CVs), galvanostatic charge/discharge (GCD), and cycling stability. Nyquist plots were collected in a

frequency range of 10^{−2}–10⁵ Hz at the open-circuit voltage with an AC amplitude of 5 mV. The conductivity of the electrolyte was measured by the EIS technique. The electrolyte was sealed in a small stainless-steel cell during the conduction measurement. The proton conductivity was calculated through equation (3) expressed as:

$$\sigma = L/R_e S \quad (3)$$

where σ , L , R_e , and S represent the proton conductivity, thickness of the cell, electrolyte resistance, and the contact area of the electrolyte, respectively.

The activation energy (E_a) of 52 wt% H₃PO₄ was estimated according to equation (4) [34], using the data of the temperature-dependent proton conduction.

$$\ln(\sigma T) = \ln\sigma_0 - E_a/k_B T \quad (4)$$

where σ_0 , k_B , and T represent the pre-exponential factor, Boltzmann constant, and temperature (K), respectively.

The areal specific capacitance (C_a) of the electrodes and SCs was calculated through equation (5):

$$C_a = I\Delta t/A\Delta U \quad (5)$$

where I , Δt , A , and ΔU represent the current (ampere, A), discharge time (second, s), geometric surface area (cm²), and output voltage (volt, V), respectively.

The volumetric specific capacitance (C_v) was calculated through equation (6):

$$C_v = \rho I\Delta t/m\Delta U \quad (6)$$

where ρ is the packing density of the active material (g cm^{−3}), and m is the loading mass of the active material (mg cm^{−2}).

The specific energy and specific power of SC devices were calculated through equations (7) and (8):

$$E = CU^2/7.2 \quad (7)$$

$$P = 3600E/\Delta t \quad (8)$$

3. Results and discussion

3.1. Structure, composition, and morphology

The GaN microcrystals were prepared by a KNO₃-mediated carbo-thermal reduction approach (Fig. 1a), through which the crystallinity, intensity ratio of lattice planes, morphology, surface chemistry, and textural properties of the samples can be tuned by controlling the annealing time. The diffraction peaks can be indexed to the (100), (002), (101), (102), (110), (103), (112), and (201) planes of wurtzite GaN (PDF# 50–0792) (Fig. 1b). Two interesting findings can be obtained from Fig. 1b: (i) the crystallinity of GaN-t is greatly improved when KNO₃ is introduced; and (ii) the intensity ratios of (002) to (100) ($I_{(002)}/(100)$) and (101) to (100) ($I_{(101)}/(100)$) are adjusted by changing the annealing time (Fig. 1b, inset). The enhanced crystallinity of GaN-t is attributed to the exothermic contribution of the reaction of KNO₃ with carbon nitride (equation (9)). The carbon nitride is derived from the decomposition of melamine at ca. 550 °C [35], at which the decomposition of KNO₃ to KNO₂ would not occur [36]. The standard molar reaction enthalpy ($\Delta_rH_m^\circ$) of equation (9) is calculated to be −35.9 kJ mol^{−1}, confirming an exothermal reaction. The changes in $I_{(002)/(100)}$ and $I_{(101)/(100)}$ indicate the lattice planes of GaN can be tuned as the (100), (002), and (101) planes are predominant in the XRD spectrum. Compared with pGaN, GaN-t manifest enhanced $I_{(002)/(100)}$ and $I_{(101)/(100)}$. This result means more atomic arrays that make up the (002) and (101) planes are present on the surface of GaN-t.

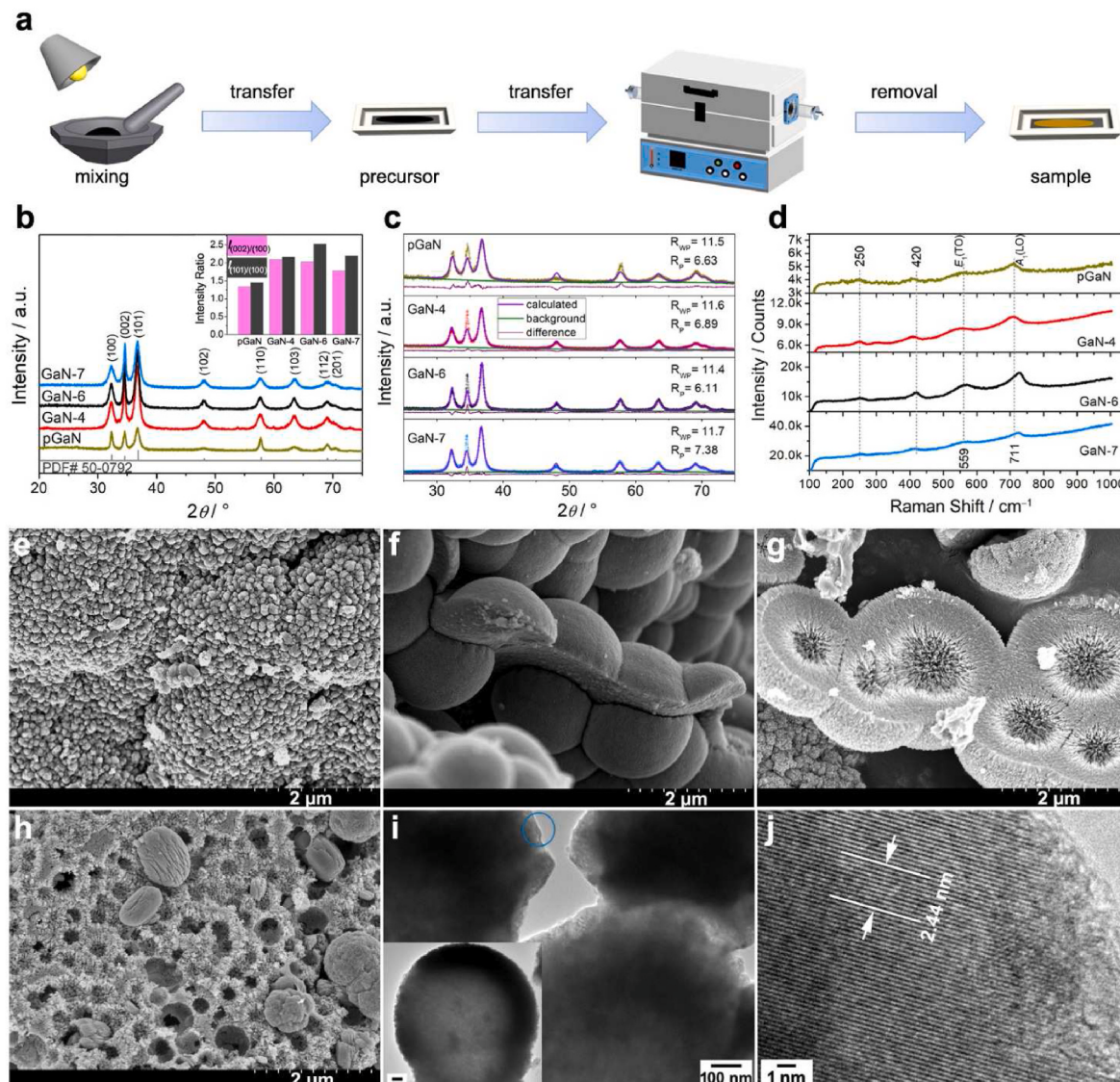
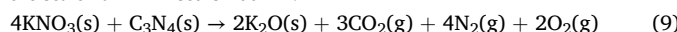


Fig. 1. (a) flow chart for sample preparation; (b) XRD pattern, inset in a is the intensity ratios of $I_{(002)/(100)}$ and $I_{(101)/(100)}$; (c) XRD pattern derived by Rietveld refinements; (d) Raman spectra; and SEM (e–h) and TEM (i,j) images of (e) pGaN; (f) GaN-4; (g) GaN-6; (h) GaN-7; (i,j) GaN-6; j corresponds to the circled area in i; the scale bar in i inset is 200 nm.



Among GaN-*t*, the crystallinity of GaN-4 is the uppermost, according to the diffraction intensity of (100), (002), and (101) planes. With increasing the annealing time to 6 and 7 h, the crystallinity of GaN-*t* is gradually decreased. This result is assigned to the dissociation of GaN, due to its thermal instability [37–39]. Further structural information is revealed by Rietveld refinements of the XRD spectra (Fig. 1c and Table S1). The *c/a* ratios are increased for GaN-*t* as compared with pGaN, in concert with the result derived from the XRD spectra (Fig. 1b, inset). In addition, the density of GaN-*t* is decreased as the annealing time increases, due to the continuous GaN dissociation. It should be pointed out that the crystallinity of GaN does not linearly increase with increasing the KNO₃ concentration in the precursor. With the same annealing time of 6 h, the crystallinity of GaN increases as the K/Ga ratio increases from 1:9 to 1:4, and then decreases with further increasing the K/Ga ratio to 3:7 (Fig. S1). This result is due to the excess consumption of nitrogen source by KNO₃ as the dosage of KNO₃ increases (equation (9)), resulting in the reduced supply of active nitrogen (N^{*}) for GaN growth. On the other hand, high-concentration KNO₃ in the precursor may function as a diluent, which obstructs the chemical combination of Ga with N^{*}, leading to a further decrease in crystallinity.

The dissociation of GaN generates defects in the samples, as revealed by the Raman spectra (Fig. 1d). The Raman peaks centered at 250, 420, 559 and 711 cm⁻¹ can be assigned to the zone-boundary phonon, acoustic phonon overtone, E₁(TO), and A₁(LO) [40], respectively. The former two peaks are not allowed by the C_{6v}⁴ space group in the first-order Raman scattering [40]. Their appearance confirms the existence of the surface disorders [38,40]. Compared with pGaN and GaN-4, the shift in the peak position of A₁(LO) to higher wavenumbers for GaN-6 and GaN-7 is attributed to the phonon coupling that occurs in their porous structures [41,42].

The dissociation of GaN is confirmed by the SEM images. pGaN is composed of aggregated nanoparticles with size concentrated at 130–220 nm (Fig. 1e), while GaN-4 is composed of micro-hemispheres with diameter centered at 1.2–2.0 μm (Fig. 1f). With increasing the annealing time to 6 h, the micro-hemispheres of GaN-6 is constituted by clusters of nanowires with thicker ends at the periphery and thinner ends at the center (Fig. 1g). The clusters of GaN nanowires preferentially dissociates at the thinner ends, which possess relatively higher surface energy as a result of the small size effect [43], leading to the formation of bowl like GaN (BL-GaN) microcrystals. The BL-GaN microcrystals

continue to dissociate and are fused with increasing the annealing time to 7 h (Fig. 1h). The porous feature of GaN-6 and GaN-7 is responsible for the shift of A₁(LO) to higher energies in the Raman spectra (Fig. 1d). The GaN microcrystals and the surface disorders can be revealed by the TEM images (Fig. 1i and j). The lattice distance of ca. 0.244 nm signals the (101) plane of wurtzite GaN (PDF# 50-0792). The discontinuous lattice fringes at the periphery of the GaN microcrystal confirm the existence of surface disorders (Fig. 1j).

In addition to the annealing time, the morphology of GaN is also dependent on the K/Ga ratio. With decreasing the K/Ga ratio to 1:9, GaN-6/1/9 is composed of nascent flower-like clusters constituted by nanoparticles with anisotropic growth (Fig. S2a). As the K/Ga ratio is increased to 3:7, GaN-6/3/7 is dominated by submicron spheres with size concentrated at 0.39–0.59 μm (Fig. S2b). The submicron spheres are constituted by nanoparticles with size smaller than 50 nm, presenting a rough surface. In this case, the molten KNO₃ (m.p. 339.2 °C [44]) liquid drops may serve as the template for the growth of GaN submicron spheres during the annealing treatment.

As the energy storage of SC electrodes is dominated by the electrochemical double layer capacitance (EDLC) at the electrode/electrolyte interface, the surface chemistry of the samples was revealed by the XPS technique. The survey XPS spectra present elemental C, N, O, and Ga (Fig. S3). No elemental K can be discerned. This result means the KNO₃-mediated carbothermal synthesis does not allow K doping in the GaN matrix, due to the larger ionic radius of K⁺ (133 p.m.) compared with Ga³⁺ (62 p.m.). The nonexistence of K is confirmed by the K 2p spectra (Fig. 2a), where there are no peaks at ca. 293.0 and 295.8 eV corresponding separately to K 2p_{3/2} and K 2p_{1/2} [45]. The existence of C indicates the remnant of carbon in the GaN samples. According to the subtraction method, the weight percents of the carbon are estimated to be 18.9 %, 3.1 %, 2.5 %, and 1.0 % for pGaN, GaN-4, GaN-6, and GaN-7 in sequence.

The other three elements are confirmed by the Ga 3d (Fig. 2b), N 1s (Fig. 2c), and O 1s spectra (Fig. 2d). In Ga 3d spectra, the peaks centered at 19.75 ± 0.05, 20.25 ± 0.05, and 20.85 ± 0.05 eV correspond to the Ga–N, Ga–O, and Ga–OH components [46,47]. The N 1s spectra can be fit into five components centered at 394.4, 396.45 ± 0.05, 397.6, 398.65 ± 0.05, and 400.7 eV, corresponding to the nitrogen defects (N_d), N–Ga, pyridinic N, N–Ga–O, and graphitic N [39,48,49]. With prolonging the annealing time, the concentrations of Ga–O and N_d increase, while the

concentrations of N–Ga and N related to carbon decrease (Table S2). These results mean the KNO₃-mediated carbothermal synthesis tends to generate more N_d sites and more oxide components in GaN-t as the annealing time prolongs, due to the release of O₂ by the reaction of KNO₃ with carbon nitride (equation (9)). As is documented in the literature, the N_d sites are adverse to the adsorption of H₃O⁺ on the surface of GaN-based electrodes, leading to reduced specific capacitance [46].

Also, the specific surface area (S_{BET}) and porous structures have important effects on the electrode performance. In this sense, the textural properties of the samples were characterized. The abrupt increase in the nitrogen sorption isotherms at the P/P^* of 0–0.01 indicates the microporous characteristic of pGaN, GaN-6, and GaN-7. The hysteresis loops in the P/P^* range of 0.4–0.98 mean the existence of meso- and macropores (Fig. 2e). The pores are concentrated at 0.79–7.46 nm (Fig. 2f). The pores for GaN-4 are dominated by mesopores centered at 2.77 nm, while micropores peaked at 0.79, 1.18, 1.44, and 1.70 nm are rich in the other three samples. Among the samples, GaN-4 manifests the smallest S_{BET} (13.8 m² g⁻¹) while GaN-6 presents the largest S_{BET} (205.1 m² g⁻¹), higher than that (166.6 m² g⁻¹) of pGaN. With prolonging the annealing time to 7 h, the S_{BET} of GaN-7 is dramatically decreased to 42.2 m² g⁻¹. Note that the specific surface area contributed by the micropores ($S_{\text{micropore}}$) dominates the S_{BET} of GaN-6, accounting for ca. 77.7 %. This is much higher than that of 34.4 % and 4.3 % for GaN-7 and GaN-4 (Table S3). These results mean the textural properties of GaN-t can be adjusted through controlling the annealing time, in addition to the morphology, crystallinity, and lattice planes. GaN-6 with large S_{BET} and hierarchical pores is expected to manifest enhanced electrode performance.

3.2. Electrochemical performance of GaN electrodes in a three-electrode system

The performance of the GaN electrodes was examined by a three-electrode system at room temperature, with electrode material being ca. 3.5 mg cm⁻². The anodic/cathodic peaks at 0–0.065/(0.14–0.026) V signal the pseudocapacitance contributed by the faradaic reactions (equations (10) and (11)). The quasi-rectangular shapes of the cyclic voltammograms (CVs) mean the EDLC dominates the total capacitance of the electrodes (Fig. 3a).

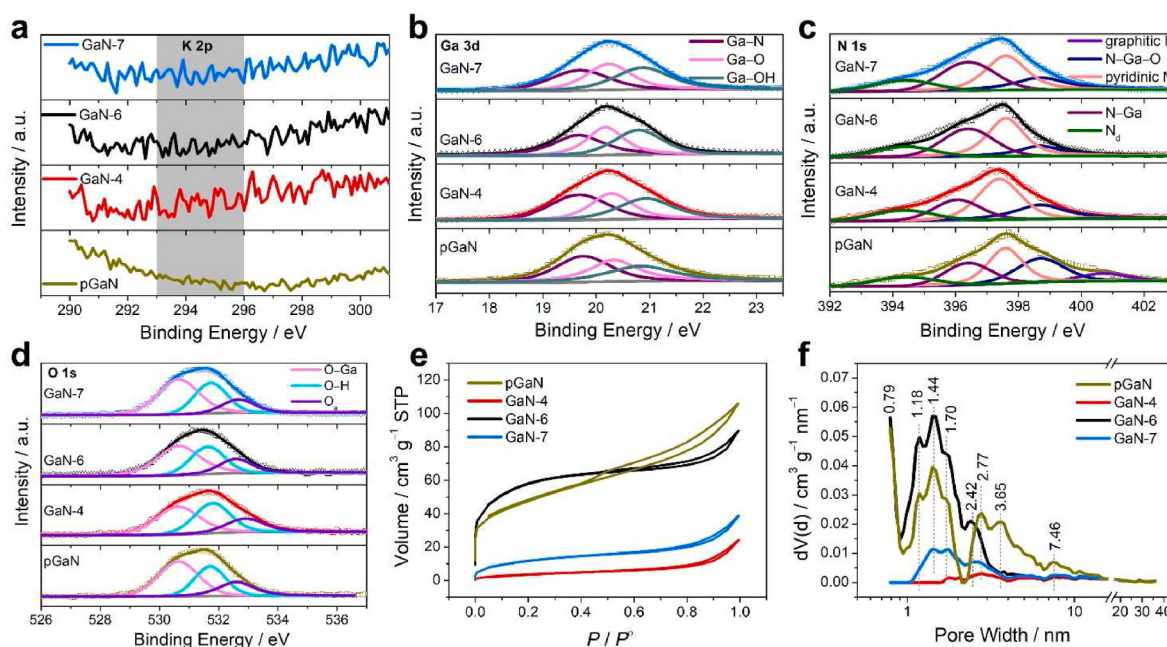


Fig. 2. (a) K 2p; (b) Ga 3d; (c) N 1s; (d) O 1s; (e) nitrogen sorption isotherms; (f) pore size distribution plots.

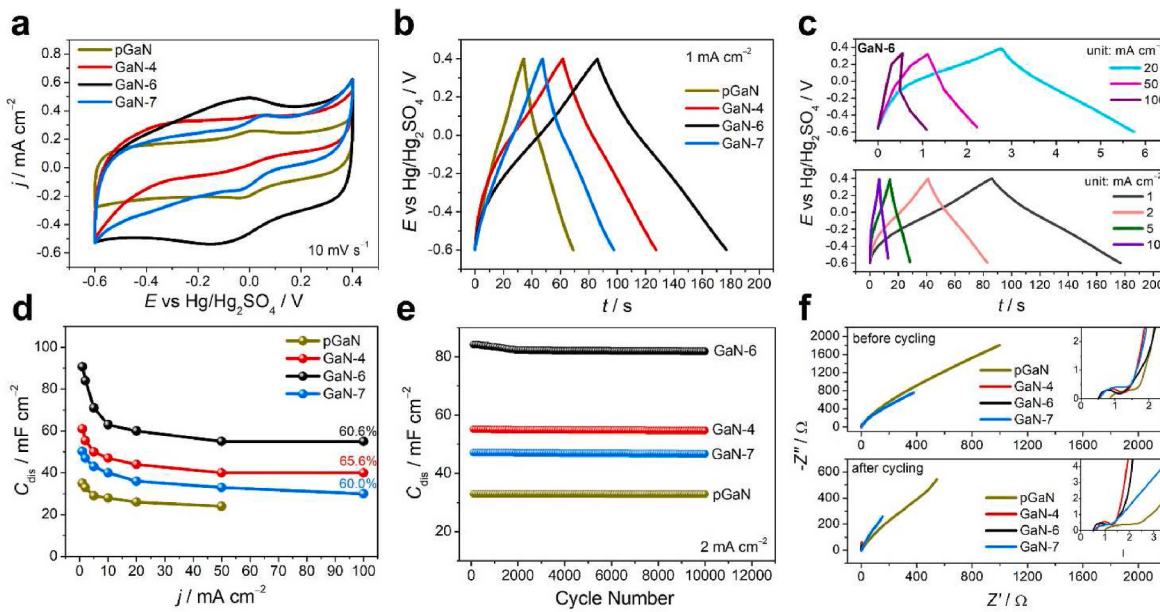
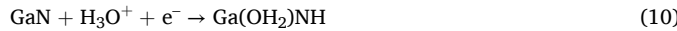


Fig. 3. Electrochemical performance of GaN electrodes: (a) CVs; (b) GCD curves at 1 mA cm^{-2} ; (c) GCD curves of GaN-6; (d) rate plots; (e) cycling plots; (f) Nyquist plots before and after cycling.



At 1 mA cm^{-2} , pGaN, GaN-4, GaN-6, and GaN-7 deliver the areal discharge specific capacitance (C_{dis}) of 35, 61, 91, and 50 mF cm^{-2} (Fig. 3b). GaN-t manifests enhanced C_{dis} at all the current densities as compared to pGaN, in particular for GaN-6 (Fig. 3c and d). The capacitance retention of GaN-t is higher than 60 % when the current density increases by two orders of magnitude, showing excellent rate performance (Fig. 3d). The C_{dis} and rate performance of GaN-t are superior to or comparable with those of carbon-, metal nitride-, and metal oxynitride-based electrodes (Table S4) [6,50–58]. These results mean the KNO_3 -mediated carbothermal synthesis facilitates to improve the electrode performance. Further, all the samples manifest excellent cycling performance (Fig. 3e), due to the structural stability of GaN. After 10,000 cycles at 2 mA cm^{-2} , pGaN, GaN-4, GaN-6, and GaN-7 retain C_{dis} of 33, 55, 82, and 47 mF cm^{-2} , presenting nearly 100 % capacitance retention. The high cycling performance of the electrodes can be reflected by the Nyquist plots (Fig. 3f), where the absolute values for the changes in equivalent series resistance (ESR) and charge transfer resistance (R_{ct}) are only $0.01\text{--}0.49 \Omega$ before and after cycling (Table S5). Note that the absolute ΔR_{ct} values for GaN-t ($0.02\text{--}0.09 \Omega$) are much smaller than that of pGaN (0.49Ω), indicating improved electrode kinetics of the former.

Of all the electrodes, GaN-6 delivers enhanced C_{dis} compared with the other three electrodes. The reason is apparently attributed to the higher S_{BET} and V_{total} pore predominantly contributed by the micropores (Table S3). As the radii of H_3O^+ and solvation shell approximate to 0.12 and 0.19 nm [59,60], the protonated water clusters, such as H_3O^+ , H_5O_2^+ , and H_9O_4^+ , can fluently enter the micropores concentrated at 0.79 and 1.44 nm without desolvation, leading to an effective use of the micropores. Also known in the literature [61,62], the ion size approximate to that of the micropores tends to yield a maximum EDLC. Note that GaN-4 with the highest crystallinity and the smallest S_{BET} and V_{total} pore exhibits the best rate capability (Fig. 3d). This result means there are other factors that influence the electrode performance (discussion below).

3.3. Charge storage mechanism and electrode kinetics

As GaN-6 manifests enhanced C_{dis} at $1\text{--}100 \text{ mA cm}^{-2}$, the charge storage mechanism is further analyzed. To explore the charge storage mechanism, GaN-6 was comparatively tested in acid, neutral, and organic solutions (Fig. 4a). At 1 mA cm^{-2} , GaN-6 delivers C_{dis} of 53 mF cm^{-2} when operating in $1 \text{ M Na}_2\text{SO}_4$, accounting for 58.2 % of that operated in $1 \text{ M H}_2\text{SO}_4$. The large difference in C_{dis} is assigned to the pseudocapacitance resulting from the faradaic reactions between GaN and H_3O^+ (equations (10) and (11)), as the ionic size of the protonated water cluster ($\text{H}_3\text{O}^+\text{-}3\text{H}_2\text{O}$) is similar to that of the sodium hydrate ion ($\text{Na}^+\text{-}3\text{H}_2\text{O}$) [59,63]. To eliminate the influence of H_3O^+ that results from the ionization of water, GaN-6 was tested in 0.5 M LiClO_4 acetonitrile solution, presenting C_{dis} of 46 mF cm^{-2} at 1 mA cm^{-2} . Assuming the C_{dis} of the electrode operated in the organic electrolyte is all from the EDLC, the pseudocapacitance of GaN-6 occupies ca. 49.5 % of the total capacitance at 1 mA cm^{-2} .

The total capacitance of the electrode can be kinetically divided into two parts contributed by diffusion-controlled process and surface capacitive behavior, respectively, especially for the electrode with porous characteristic. According to $i(V) = k_1v + k_2v^{1/2}$ (equation 12) [64,65], the capacitive and diffusive contributions can be estimated by determining k_1v and $k_2v^{1/2}$, where $i(V)$ represents the current at a given potential (V) and v is the scan rate. By linear fit of the $i(V)/v^{1/2}$ vs $v^{1/2}$ plot (Fig. 4b), the two kinds of contributions are determined, using the data of anodic peak currents as a function of the scan rate (Fig. S4a). With increasing the scan rate from 10 to 500 mV s^{-1} , the diffusive capacitance is reduced from 32 % to 5 % (Fig. 4c and d). This result means GaN-6 is featured by the surface capacitive behavior. The electrode behavior is further analyzed through the equation of $i = av^b$ (equation 13), where i is the peak current of redox reactions, a and b are tunable parameters, and v the scan rate [66]. By linear fit of $\log(i)$ vs $\log(v)$ plots (Fig. 4e), the b values of GaN-6 are determined to be 0.91 and 0.90 for the cathodic and anodic peak currents vs the scan rate. The high b values confirm the surface capacitive effect governs the charge storage of GaN-6, leading to high rate capability [66].

According to the literature [67], the kinetic parameters associated with the faradaic reactions can be estimated by using the difference between the anodic and cathodic peaks (ΔE_p). When the ΔE_p is less than $60/n \text{ mV}$ at a given rate, the faradaic reaction is reversible, where n is

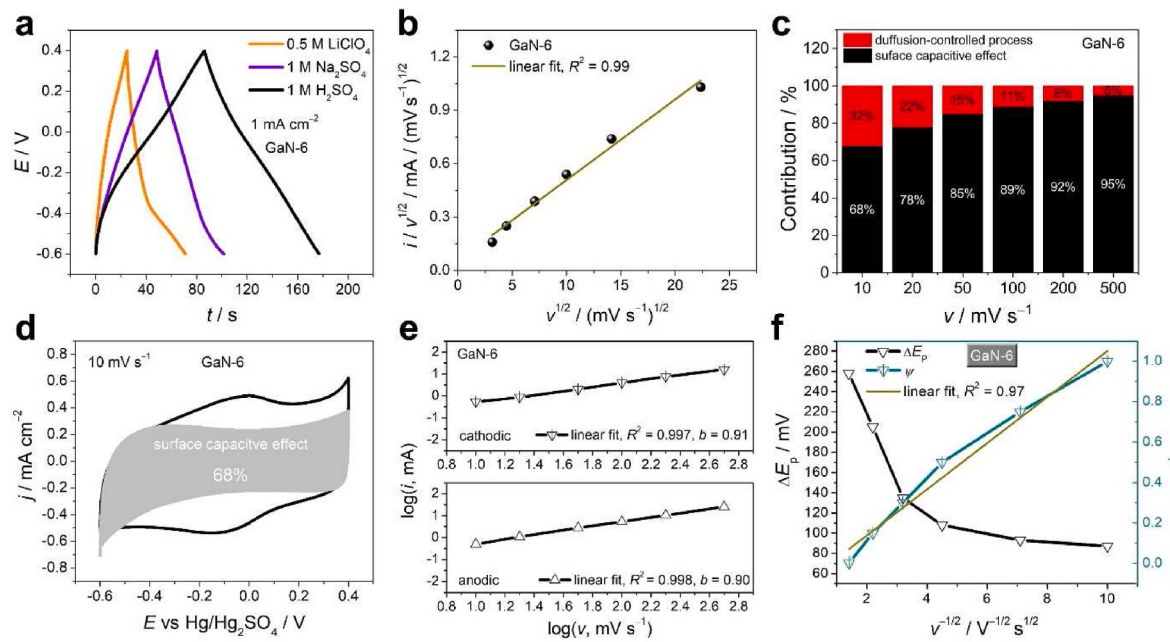


Fig. 4. Charge storage mechanism and electrode behavior of GaN-6: (a) GCD curves; (b) plot of $i/v^{1/2}$ vs $v^{1/2}$; (c) histogram of diffusive and capacitive contributions; (d) CVs; (e) plots of $\log(i)$ vs $\log(v)$; (f) Nicholson's working curve and plot of ΔE_p vs $v^{-1/2}$.

the electron number in a faradaic equation. As such, no kinetic information on the electron transport is acquired. The ΔE_p increases as the scan rate increases, and a moment may occur at which the rates of electron transport and potential change become competitive [67]. At this moment, the ΔE_p is higher than $60/n$ mV. Using the equation of $\psi = k^0(RT/\pi nFD)^{1/2}v^{-1/2}$ (equation 14) [64], the kinetic information on the faradaic reactions can be acquired, where ψ , k^0 , and D represent the dimensionless Nicholson's parameter, reaction rate constant, and proton diffusion coefficient ($3.625 \times 10^{-3}RT/F, \text{ cm}^2 \text{ s}^{-1}$) [68], and the other parameters have their usual meanings. For GaN electrodes, n equals 1 based on the faradaic reactions (equations (10) and (11)). By converting ΔE_p higher than 60 mV into ψ ($0.001 < \psi < 7$) [67], Nicholson's working curves are obtained through plotting ψ vs $v^{-1/2}$ (Fig. 4f and Figs. S4b-d). Thus, the k^0 for GaN-6 is estimated to be $1.37 \times 10^{-3} \text{ cm s}^{-1}$, higher than that of 1.24×10^{-3} and $6.82 \times 10^{-4} \text{ cm s}^{-1}$ for GaN-7 and pGaN yet lower than that of $1.82 \times 10^{-3} \text{ cm s}^{-1}$ for GaN-4. The physical meaning of k^0 is a measure of kinetic ability including charge and mass transport. Systems with higher k^0 reach reaction equilibrium faster than those with lower k^0 [64]. Thus, the highest k^0 of GaN-4 is responsible for the best rate performance, although GaN-4 has the lowest S_{BET} and $V_{\text{total pore}}$ among the electrodes (Table S3). One reason for the highest k^0 of GaN-4 is attributed to the lower Ga-O/Ga-OH and N_d concentrations, which are adverse to H_3O^+ adsorption [46]. The second reason is attributed to the highest crystallinity, which facilitates to improve the electrode kinetics and reduces the charge transfer resistance [69,70]. Such a situation is confirmed by the EIS measurements, as shown in Fig. 3f and Table S5. As for GaN-7, the highest concentrations of Ga-O/Ga-OH and N_d , the smaller S_{BET} and $V_{\text{total pore}}$, and the reduced crystallinity among GaN-t cooperatively act on the electrode, leading to a lower k^0 and hence inferior rate capability.

3.4. Correlating theoretical computations with experimental results

As discussed above, the crystallinity, lattice planes, surface chemistry, textural properties, and hence electrode performance can be adjusted through controlling the annealing time of the KNO_3 -mediated synthesis. It is not difficult to comprehend GaN-6 with the largest S_{BET} , hierarchical pores, and second highest crystallinity manifests superior performance. A noteworthy point is that GaN-4 having the smallest S_{BET}

and $V_{\text{total pore}}$ yet the uppermost crystallinity and enhanced $I_{(002)/(100)}$ and $I_{(101)/(100)}$ yields the highest k^0 and hence the best rate performance. This result means the enhanced $I_{(002)/(100)}$ and $I_{(101)/(100)}$ are essential for improving the electrode performance, in addition to the fewer Ga-O/Ga-OH and N_d sites and the high crystallinity.

To clarify this point, theoretical computations were performed, as shown in Fig. 5. Although protons in water exist in the form of $H^+(H_2O)_n$ clusters [60,71], we first chose H_3O^+ , the simplest proton hydrate, as a probe to reveal the adsorption behaviors of GaN planes for protons in acid solution (Fig. 5a-g). An interesting finding is that H_3O^+ does not dissociate upon the (002) plane, but dissociates once and twice upon the (101) and (100) planes, respectively. From the viewpoint of energy, the adsorption energy of (002) is higher than that of (100) and (101) before the dissociation of H_3O^+ (Fig. 5g). These results suggest (i) the pseudocapacitance contributed by the faradaic reactions (equations (10) and (11)) results from the spontaneous dissociation of H_3O^+ upon GaN (100) and (101) planes; (ii) compared with pGaN, the enhanced performance of GaN-t is closely related to their surface atomic structures composed by atomic arrays that make up the (002) plane, which is more active in adsorbing H_3O^+ . However, it remains difficult to comprehend the better performance of GaN-t, because the $I_{(101)/(100)}$ values of GaN-4 (2.16), GaN-6 (2.53), and GaN-7 (2.19) are higher than that of pGaN (1.46) (Fig. 1b, inset).

To reveal the underlying mechanism, we further examined the adsorption behaviors of GaN (100), (002), and (101) planes for H^+ (Fig. 5h-n) [17], as the proton hydrates tend to desolvate in the inner Helmholtz layer to form an electric double layer at the electrode/electrolyte interface [72,73]. The computational results show the adsorption energies of (002) and (101) planes are much higher than that of (100) plane, in particular for the (002) plane (Fig. 5n). This is confirmed by the charge accumulation (yellow) and depletion (cyan) result, where more charge is transferred to H^+ from N (Fig. 5l), in comparison with that of (100) and (101) planes (Fig. 5k,m). Even for H^+ captured by surface Ga atoms, the adsorption energy of (002) plane is higher than that of (101) and (100) planes in turn (Fig. 5s). The computational results mean the (002) and (101) planes are more active in adsorbing H^+ , compared with the (100) plane. Thus, it can be understood that (i) GaN-t with enhanced $I_{(002)/(100)}$ and $I_{(101)/(100)}$ manifest improved electrochemical performance compared with pGaN; (ii) GaN-4

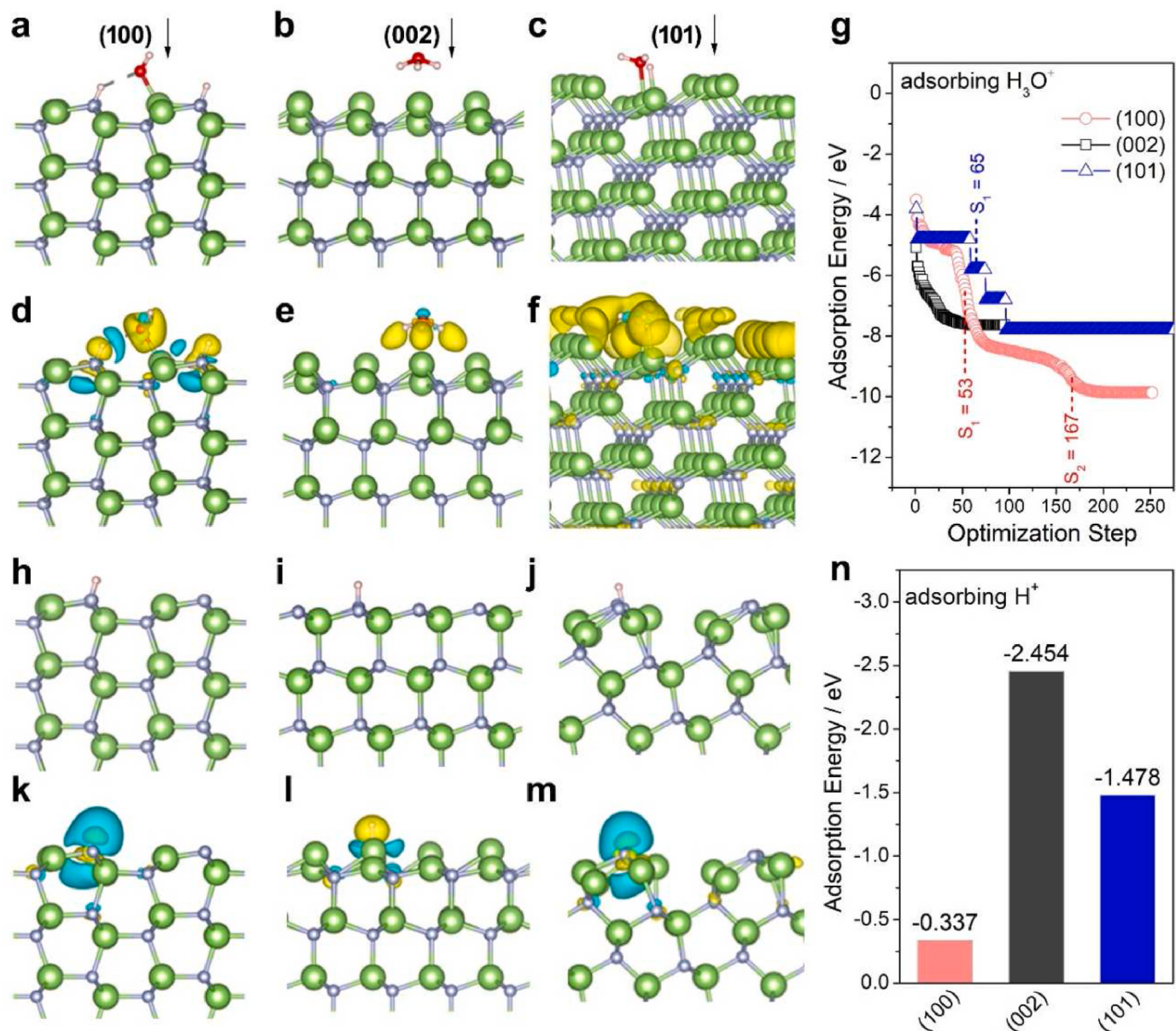


Fig. 5. Theoretical computation results of the adsorption of GaN (100), (002), and (101) for H_3O^+ (a–g) and H^+ (h–n): (a–c) and (h–j) final configurations; (d–f) and (k–m) charge-density difference; (g) plots of adsorption energy for H_3O^+ as a function of the optimization step; (n) adsorption energy for H^+ ; S_1 and S_2 in g denote the first and second dissociation steps; the green and gray spheres denote the Ga and N atoms, respectively. (For interpretation of the references to colour in this figure legend, the reader is referred to the Web version of this article.)

with the highest $I_{(002)/(100)}$ and crystallinity presents the best rate performance.

3.5. Electrochemical performance of GaN microcrystal-based symmetric SCs

To meet the requirement on the loading mass of electrodes for commercial SCs [25], GaN-6||GaN-6 symmetric SCs were assembled with a loading mass of 10 mg cm^{-2} on a single electrode, using 52 wt% H_3PO_4 as the electrolyte. The reasons for choosing 52 wt% H_3PO_4 as the electrolyte are (i) the ESW of the electrolyte can be enlarged to ca. 1.6 V by setting the onset current at 0.07 mA for oxygen evolution reaction (OER) in the linear sweep voltammetry (LSV) curve (Fig. S6a); (ii) the overall conductivity of the electrolyte reaches a maximum among the H_3PO_4 aqueous solutions [18]. The characterizations of the electrolyte are provided in the Supplementary material. The results show (i) the

water activity of the electrolyte is reduced due to the confinement of water molecules by H_3PO_4 species, as proved by the FT-IR (Fig. S6b) and Raman spectra (Fig. S6c), leading to an enlarged ESW; (ii) the anti-freezing property of the electrolyte is good as the endothermic peak corresponding to the freezing point is centered at -23.9°C (Fig. S6d). The enlarged ESW and good anti-freezing ability of the electrolyte enable enhanced specific energy and wide-temperature performance of the SCs.

At 10 mV s^{-1} , the CVs of the SCs present a rectangular shape, especially at subzero temperatures (Fig. 6a). As the temperature decreases, the peak current density for OER decreases. These results mean the water activity of the electrolyte is further suppressed at subzero temperatures while increased with increasing temperature. As the temperature increases from -60 to 45°C the CV areas increase. With a further increase of the temperature to 60°C , the CV area decreases. This result means the specific capacitance of the SC can be improved by

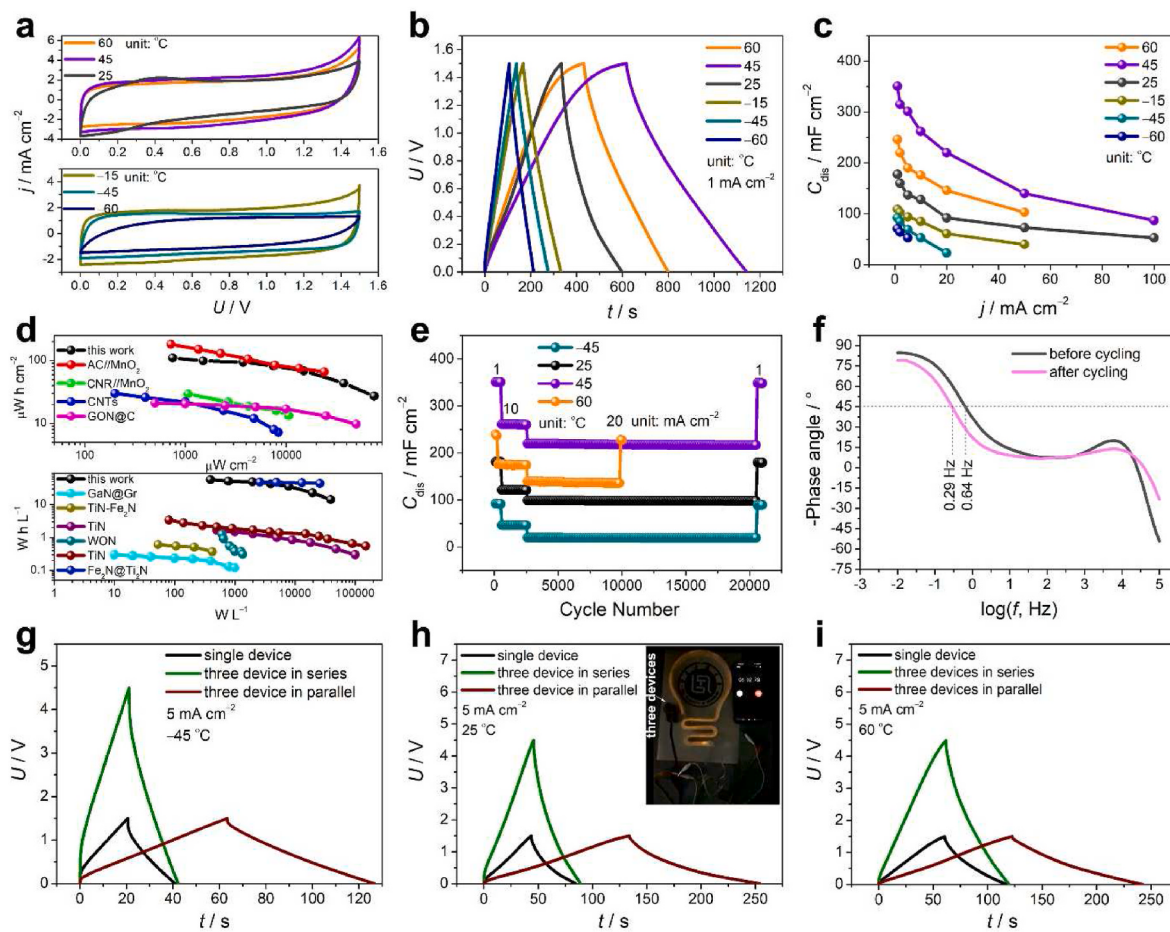


Fig. 6. Electrochemical performance of the GaN-6||GaN-6 SCs: (a) CVs; (b) GCD curves; (c) rate plots; (d) Ragone plots; (e) cycling plots; (f) Bode plots; and GCD curves of three devices in series and parallel operating at: (g) -45°C ; (h) 25°C ; (i) 60°C ; inset in h is the snapshot of a neon light belt lightened by three devices in series, taken at $6'02''$ and room temperature.

increasing the temperature to 45°C while deteriorates with further increasing the temperature to 60°C . The former is attributed to the enhanced proton conductivity of the electrolyte with increasing temperature, as reflected by the Nyquist plots (Fig. S7a). Such a situation enables more ions to reach the electrode/electrolyte interface per unit of time. The latter is attributed to the reduced proton conductivity, due to the obstruction of ion migration by enhanced molecular thermal motion at the temperature increases to 60°C . The phenomenon that the specific capacitance first increases and then decreases is confirmed by the GCD measurements.

At 1 mA cm^{-2} , the C_{dis} of the SC increases from 71 to 351 and then decreases to 246 mF cm^{-2} as the temperature increases from -60 to 45 and then to 60°C (Fig. 6b). The capacitance sequence retains with increasing the current density (Fig. 6c). When operating at 50 mA cm^{-2} and 45°C , the SC delivers C_{dis} of 140 mF cm^{-2} , higher than that of 103 and 73 mF cm^{-2} for the SC operating at 60 and 25°C in sequence. At -45°C , the C_{dis} of the SC at 10 mA cm^{-2} is 53 mF cm^{-2} . Even at -60°C , the SC still manifests C_{dis} of 53 mF cm^{-2} at 5 mA cm^{-2} . The reliable operation of the SC devices at temperatures below the freezing point is attributed to that proton transport still proceeds through ion transport channels within the ice lattice [74,75], as proved by the Nyquist plots (Fig. S7). As the packing density of GaN-6 is calculated to be 5.23 g cm^{-3} (Fig. S8), the SC at 1 mA cm^{-2} delivers volumetric specific capacitance (C_v) of 93 and 184 F cm^{-3} at room temperature and 45°C , respectively. Even at 100 mA cm^{-2} and 45°C , the SC can deliver C_v of 46 F cm^{-3} . The specific energy of the SC can reach $109.7 \text{ } \mu\text{Wh cm}^{-2}$ and 57.4 Wh L^{-1} at the specific power of $750 \text{ } \mu\text{W cm}^{-2}$ and 392.2 W L^{-1} . Even at the specific

power of 75 mW cm^{-2} and 39.2 kW L^{-1} , the SC can deliver the specific energy of $27.2 \text{ } \mu\text{Wh cm}^{-2}$ and 14.2 Wh L^{-1} . The $E-P$ performance of the SC is comparable with or superior to that of the counterparts assembled by active carbon (AC)||MnO₂ [50], carbon nanorods (CNR)||MnO₂ [51], carbon nanotubes (CNTs) [52], gallium oxynitride (GON)@carbon cloth [53], GaN nanowires@graphite (Gr) paper [6], TiN-Fe₂N [54], corn-like TiN [55], holey tungsten oxynitride nanowires (WON) [56], TiN paper [57], and Fe₂N@Ti₂N [58] (Fig. 6d).

By changing the current density from 1 to 20 and then to 1 mA cm^{-2} (Fig. 6e), the SCs operating at 45 , 25 , and -45°C retain C_{dis} of 349 , 179 , and 90 mF cm^{-2} after 21,000 cycles, showing nearly 100 % capacitance retention. When operating at 60°C for 10,000 cycles with varied current densities, the SC delivers C_{dis} of 228 mF cm^{-2} , presenting 95 % capacitance retention. The high cycling stability of GaN-6 can be reflected by the XRD and SEM results. After 21,000 cycles with varied current densities at room temperature, there is no shift in the peak position of the XRD spectra, although the crystallinity of the diffraction peaks is slightly depressed (Fig. S9a). Also, the GaN microcrystals retain their bowl-like morphology with mild pulverization (Figs. S9b-e). In addition, the absolute values for ΔESR and ΔR_{ct} are only 2.4 and 0.8Ω , according to the Nyquist plots before and after 21,000 cycles at room temperature (Fig. S7). The excellent capacitive performance of the SC is confirmed by the Bode plots (Fig. 6f). The phase angles in the low-frequency region are ca. -85° and -80° before and after cycling at room temperature, approximate to that of -90° for ideal capacitors [5]. The characteristic frequency (f_0) at -45° denotes the moment at which the capacitive impedance equals the resistive impedance [55]. Thus, the time constant

$(\tau_0, \tau_0 = 1/f_0)$ of the SC device before and after cycling is estimated to be 1.6 and 3.4 s, respectively. The smaller the τ_0 , the higher the rate capability [76]. The τ_0 of the SC device is close to that of 1.7 s for aligned RGO-based SCs [76], and is greatly lower than that of 10 s for traditional activated carbon-based SCs [77]. The small τ_0 of the SC device is attributed to the cooperative effect of (i) the porous characteristic of the electrode; (ii) the enhanced $I_{(002)/(100)}$ and $I_{(101)/(100)}$ that ensure easy electrosorption of $\text{H}_3\text{O}^+/\text{H}^+$ on the GaN surface; and (iii) the 52 wt% H_3PO_4 that provides a Grotthuss mechanism for fast proton conduction (Fig. S10) [78], leading to high rate capability. The high wide-temperature performance of the SC devices warrants their real application in extreme environments.

To apply the SC devices in practice, three devices were assembled in series and parallel for electrochemical testing at -45, 25, and 60 °C. Three devices in series and parallel can output a voltage of 4.5 V and discharge time three times that of a single device, respectively (Fig. 6g-i). Also, a neon light belt (4.5 V, 1 A) can be lightened for more than 1.5, 6, and 1.5 min by three devices in series operating at -45, 25, and 60 °C, respectively (Fig. 6h inset and Videos S1,2), confirming the feasibility of the SC devices applied in the environments with significant temperature changes. In addition, the assembled SC device manifests a low leakage current (I_{lc}). The I_{lc} sharply decreased from 5.34 mA to 238 μA after 5.2 min, and then stabilizes at 238–215 μA during the following self-charging process (Fig. S11). The GaN-microcrystals-based SCs with small I_{lc} hold potential for integration with other energy collectors to construct efficient self-powered systems [55].

4. Conclusion

In summary, the lattice planes and crystallinity of GaN microcrystals can be tuned by KNO_3 -mediated carbothermal synthesis, in addition to the morphology, textural properties, and surface chemistry. The adsorption behaviors of GaN (100), (002), and (101) planes for H_3O^+ and H^+ have been revealed through theoretical computations. The GaN (002) plane is more active in adsorbing H^+ and H_3O^+ compared with the GaN (101) and (100) planes, before the dissociation of H_3O^+ . The adjustment of the surface atomic structure and the enhanced crystallinity cooperatively act on the GaN electrodes, leading to enhanced performance for interfacial energy storage. Using 52 wt% H_3PO_4 as the electrolyte, the GaN microcrystal-based symmetric SCs can be reliably operated in a wide temperature range, holding promising application in the environments with significant temperature changes.

CRediT authorship contribution statement

Kai Zhou: Writing – original draft, Methodology, Investigation, Data curation. **Min Zou:** Writing – original draft, Investigation, Data curation. **Jingwen Guo:** Investigation, Data curation. **Zhen Xu:** Methodology, Data curation. **Wei Hu:** Supervision, Methodology. **Yuzhou Zhu:** Investigation, Data curation. **Libin Liu:** Funding acquisition, Formal analysis. **Ligang Gai:** Writing – review & editing, Supervision, Methodology, Funding acquisition, Data curation.

Declaration of competing interest

The authors declare that they have no known competing financial interests or personal relationships that could have appeared to influence the work reported in this paper.

Data availability

Data will be made available on request.

Acknowledgements

This work was financially supported by the Natural Science

Foundation of Shandong Province (ZR2019MEM015), and the Taishan Scholars Program and Jinan Innovation Team (202228021).

Supplementary Material

The Supplementary material contains additional data on the electrode, electrolyte, and SC devices, including XRD, SEM, XPS, FT-IR, Raman, LSV, DSC, and electrochemical data.

Appendix A. Supplementary data

Supplementary data to this article can be found online at <https://doi.org/10.1016/j.jpowsour.2024.234932>.

References

- [1] R. Adalati, M. Sharma, S. Sharma, A. Kumar, G. Malik, R. Boukherroub, R. Chandra, Metal nitrides as efficient electrode material for supercapacitors: a review, *J. Energy Storage* 56 (2022) 105912.
- [2] Y. Zhou, W. Guo, T. Li, A review on transition metal nitrides as electrode materials for supercapacitors, *Ceram. Int.* 45 (2019) 21062–21076.
- [3] J. Theerthagiri, S.J. Lee, A.P. Murthy, J. Madhavan, M.Y. Choi, Fundamental aspects and recent advances in transition metal nitrides as electrocatalysts for hydrogen evolution reaction: a review, *Curr. Opin. Solid State Mater. Sci.* 24 (2020) 100805.
- [4] I. Ashraf, S. Rizwan, M. Iqbal, A comprehensive review on the synthesis and energy applications of nano-structured metal nitrides, *Frontiers Mater.* 7 (2020) 181.
- [5] S. Wang, L. Zhang, C. Sun, Y. Shao, Y. Wu, J. Lv, X. Hao, Gallium nitride crystals: novel supercapacitor electrode materials, *Adv. Mater.* 28 (2016) 3768–3776.
- [6] S. Wang, C. Sun, Y. Shao, Y. Wu, L. Zhang, X. Hao, Self-supporting GaN nanowires/graphite paper: novel high-performance flexible supercapacitor electrodes, *Small* 13 (2017) 1603330.
- [7] M. Idrees, A. Mukhtar, R. Ataur, S.M. Abbas, Q. Zhang, X. Li, Transition metal nitride electrodes as future energy storage devices: a review, *Mater. Today Commun.* 27 (2021) 102363.
- [8] B. Gao, X. Li, K. Ding, C. Huang, Q. Li, P.K. Chu, K. Huo, Recent progress in nanostructured transition metal nitrides for advanced electrochemical energy storage, *J. Mater. Chem. A* 7 (2019) 14–37.
- [9] R. Qin, P. Wang, C. Lin, F. Cao, J. Zhang, L. Chen, S. Mu, Transition metal nitrides: activity origin, synthesis and electrocatalytic applications, *Acta Phys. - Chim. Sin.* 37 (2021) 2009099.
- [10] J.G. Chen, Carbide and nitride overlayers on early transition metal surfaces: preparation, characterization, and reactivities, *Chem. Rev.* 96 (1996) 1477–1498.
- [11] L. Zhou, K. Zhang, Z. Hu, Z. Tao, L. Mai, Y.-M. Kang, S.-L. Chou, J. Chen, Recent developments on and prospects for electrode materials with hierarchical structures for lithium-ion batteries, *Adv. Energy Mater.* 8 (2018) 1701415.
- [12] P. Simon, Y. Gogotsi, Capacitive energy storage in nanostructured carbon-electrolyte systems, *Acc. Chem. Res.* 46 (2013) 1094–1103.
- [13] J. Shen, Y. Wang, K. Gu, Y. Zhu, Y. Hu, C. Li, Construction of hierarchical functional nanomaterials for energy conversion and storage, *Particuology* 48 (2020) 34–47.
- [14] N. Tian, Z.-Y. Zhou, S.-G. Sun, Y. Ding, Z.L. Wang, Synthesis of tetrahedral platinum nanocrystals with high-index facets and high electro-oxidation activity, *Science* 316 (2007) 732–735.
- [15] H. Fu, L. Xiong, W. Han, M. Wang, Y.J. Kim, X. Li, W. Yang, G. Liu, Highly active crystal planes-oriented texture for reversible high-performance Zn metal batteries, *Energy Storage Mater.* 51 (2022) 550–558.
- [16] H. Cui, G. Zhu, X. Liu, F. Liu, Y. Xie, C. Yang, T. Lin, H. Gu, F. Huang, Niobium nitride Nb4N5 as a new high-performance electrode material for supercapacitors, *Adv. Sci.* 2 (2015) 1500126.
- [17] S. Xi, G. Lin, L. Jin, H. Li, K. Xie, Metallic porous nitride single crystals at two-centimeter scale delivering enhanced pseudocapacitance, *Nat. Commun.* 10 (2019) 4727.
- [18] J.P. Melchior, K.D. Kreuer, J. Maier, Proton conduction mechanisms in the phosphoric acid-water system ($\text{H}(4)\text{P}(2)\text{O}(7)\text{-H}(3)\text{PO}(4)\text{.2H}(2)\text{O}$): a (1)H, (31)P and (17)O PFG-NMR and conductivity study, *Phys. Chem. Chem. Phys.* 19 (2016) 587–600.
- [19] L. Suo, O. Borodin, T. Gao, M. Olgun, J. Ho, X. Fan, C. Luo, C. Wang, K. Xu, “Water-in-salt” electrolyte enables high-voltage aqueous lithium-ion chemistries, *Science* 350 (2015) 938–943.
- [20] X. Fan, X. Ji, L. Chen, J. Chen, T. Deng, F. Han, J. Yue, N. Piao, R. Wang, X. Zhou, X. Xiao, L. Chen, C. Wang, All-temperature batteries enabled by fluorinated electrolytes with non-polar solvents, *Nat. Energy* 4 (2019) 882–890.
- [21] X. Dong, Z. Guo, Z. Guo, Y. Wang, Y. Xia, Organic batteries operated at -70 °C, *Joule* 2 (2018) 902–913.
- [22] S. Lv, S. Wang, T. Wang, L. Liu, J. Yu, T. Dong, G. Wang, Z. Wang, C. Liang, L. Li, X. Xu, L. Zhang, Vacancy-modified few-layered GaN crystal for novel high-temperature energy storage, *J. Mater. Chem. A* 10 (2022) 22007–22015.
- [23] Q. Nian, J. Wang, S. Liu, T. Sun, S. Zheng, Y. Zhang, Z. Tao, J. Chen, Aqueous batteries operated at -50 °C, *Angew. Chem. Int. Ed.* 58 (2019) 16994–16999.

- [24] C.S. Rustomji, Y. Yang, T.K. Kim, J. Mac, Y.J. Kim, E. Caldwell, H. Chung, Y. S. Meng, Liquefied gas electrolytes for electrochemical energy storage devices, *Science* 356 (2017) eaal4263.
- [25] H. Sun, L. Mei, J. Liang, Z. Zhao, C. Lee, H. Fei, M. Ding, J. Lau, M. Li, C. Wang, X. Xu, G. Hao, B. Papandrea, I. Shakir, B. Dunn, Y. Huang, X. Duan, Three-dimensional holey-graphene/nobia composite architectures for ultrahigh-rate energy storage, *Science* 356 (2017) 599–604.
- [26] Y. Xia, T.S. Mathis, M.Q. Zhao, B. Anasori, A. Dang, Z. Zhou, H. Cho, Y. Gogotsi, S. Yang, Thickness-independent capacitance of vertically aligned liquid-crystalline MXenes, *Nature* 557 (2018) 409–412.
- [27] J. Buha, I. Djerdj, M. Antonietti, M. Niederberger, Thermal transformation of metal oxide nanoparticles into nanocrystalline metal nitrides using cyanamide and urea as nitrogen source, *Chem. Mater.* 19 (2007) 3499–3505.
- [28] Y. Nitta, M. Yoshimura, K. Nishinari, The effect of thermal history on the elasticity of K-type gellan gels, *Carbohydr. Polym.* 113 (2014) 189–193.
- [29] W. Kohn, L.J. Sham, Self-consistent equations including exchange and correlation effects, *Phys. Rev.* 140 (1965) A1133–A1138.
- [30] G. Kresse, J. Furthmüller, Efficient iterative schemes for ab initio total-energy calculations using a plane-wave basis set, *Phys. Rev. B* 54 (1996) 11169–11186.
- [31] J.P. Perdew, K. Burke, M. Ernzerhof, Generalized gradient approximation made simple, *Phys. Rev. Lett.* 77 (1996) 3865–3868.
- [32] G. Kresse, D. Joubert, From ultrasoft pseudopotentials to the projector augmented-wave method, *Phys. Rev. B* 59 (1999) 1758–1775.
- [33] K. Momma, F. Izumi, VESTA 3 for three-dimensional visualization of crystal, volumetric and morphology data, *J. Appl. Crystallogr.* 44 (2011) 1272–1276.
- [34] K. Ono, M. Ishizaki, K. Kanaizuka, T. Togashi, T. Yamada, H. Kitagawa, M. Kurihara, Grain-boundary-Free super-proton conduction of a solution-processed prussian-blue nanoparticle film, *Angew. Chem. Int. Ed.* 56 (2017) 5531–5535.
- [35] S.C. Yan, Z.S. Li, Z.G. Zou, Photodegradation performance of g-C3N4 fabricated by directly heating melamine, *Langmuir* 25 (2009) 10397–10401.
- [36] M. Ravanbod, H.R. Pouretedal, Catalytic effect of Fe2O3, Mn2O3, and TiO2 nanoparticles on thermal decomposition of potassium nitrate, *J. Therm. Anal. Calorim.* 124 (2015) 1091–1098.
- [37] M.R. Lorenz, B.B. Binkowski, Preparation, stability, and luminescence of gallium nitride, *J. Electrochem. Soc.* 109 (1962) 24–26.
- [38] F. Xu, Y. Xie, X. Zhang, S. Zhang, X. Liu, W. Xi, X. Tian, Single-Crystalline gallium nitride microspindles: synthesis, characterization, and thermal stability, *Adv. Funct. Mater.* 14 (2004) 464–470.
- [39] Z. Li, X. Wu, K. Zhou, S. Wang, Q. Lu, L. Liu, Q. Ban, L. Gai, Thermal instability-induced formation of hierarchically structured porous GaN/nitrogen-doped carbon with high performance for supercapacitor, *J. Energy Storage* 72 (2023) 108434.
- [40] H.-L. Liu, C.-C. Chen, C.-T. Chia, C.-Y. Yeh, C.-H. Chen, M.-Y. Yu, S. Keller, S. P. DenBaars, Infrared and Raman-scattering studies in single-crystalline GaN nanowires, *Chem. Phys. Lett.* 345 (2001) 245–251.
- [41] T.L. Williamson, D.J. Diaz, P.W. Bohn, R.J. Molnar, Structure–property relationships in porous GaN generated by Pt-assisted electroless etching studied by Raman spectroscopy, *J. Vac. Sci. Technol. B: Microelectronic. Nanometer Struct.* 22 (2004) 925–931.
- [42] I. Tiginyanu, A. Sarua, G. Irmer, J. Monecke, S. Hubbard, D. Pavlidis, V. Valiae, Fröhlich modes in GaN columnar nanostructures, *Phys. Rev. B* 64 (2001) 233317.
- [43] W.H. Moon, H.J. Kim, C.H. Choi, Molecular dynamics simulation of melting behavior of GaN nanowires, *Scripta Mater.* 56 (2007) 345–348.
- [44] T.S. Ritchie, K.E. Riegner, R.J. Seals, C.J. Rogers, D.E. Riegner, Evolution of medieval gunpowder: thermodynamic and combustion analysis, *ACS Omega* 6 (2021) 22848–22856.
- [45] R. Sawyer, H.W. Nesbitt, R.A. Secco, High resolution X-ray Photoelectron Spectroscopy (XPS) study of K2O–SiO2 glasses: evidence for three types of O and at least two types of Si, *J. Non-Cryst. Solids* 358 (2012) 290–302.
- [46] J. Wang, X. Wu, X. Lu, Z. Xu, H. Jiang, L. Liu, Q. Ban, L. Gai, Insight into defect-engineered gallium oxynitride nanoparticle-based electrodes with improved electrochemical performance for supercapacitors, *Electrochim. Acta* 404 (2022) 139733.
- [47] C.C. Surdu-Bob, S.O. Saidi, J.L. Sullivan, An X-ray photoelectron spectroscopy study of the oxides of GaAs, *Appl. Surf. Sci.* 183 (2001) 126–136.
- [48] A. Primo, S. Navalon, A.M. Asiri, H. Garcia, Chitosan-templated synthesis of few-layers boron nitride and its unforeseen activity as a Fenton catalyst, *Chem. Eur. J.* 21 (2015) 324–330.
- [49] B. Chang, L. Li, D. Shi, H. Jiang, Z. Ai, S. Wang, Y. Shao, J. Shen, Y. Wu, Y. Li, X. Hao, Metal-free boron carbonitride with tunable boron Lewis acid sites for enhanced nitrogen electroreduction to ammonia, *Appl. Catal. B Environ.* 283 (2021) 119622.
- [50] C. Long, D. Qi, T. Wei, J. Yan, L. Jiang, Z. Fan, Nitrogen-Doped carbon networks for high energy density supercapacitors derived from polyaniline coated bacterial cellulose, *Adv. Funct. Mater.* 24 (2014) 3953–3961.
- [51] P. Shang, J. Zhang, W. Tang, Q. Xu, S. Guo, 2D thin nanoflakes assembled on mesoporous carbon nanorods for enhancing electrocatalysis and for improving asymmetric supercapacitors, *Adv. Funct. Mater.* 26 (2016) 7766–7774.
- [52] J. Park, Y.-E. Yoo, L. Mai, W. Kim, Rational design of a redox-active nonaqueous electrolyte for a high-energy-density supercapacitor based on carbon nanotubes, *ACS Sustain. Chem. Eng.* 7 (2019) 7728–7735.
- [53] J. Wang, F. Zhang, Z. Xu, W. Hu, H. Jiang, L. Liu, L. Gai, Gallium oxynitride@carbon cloth with impressive electrochemical performance for supercapacitors, *Chem. Eng. J.* 411 (2021) 128481.
- [54] C. Zhu, P. Yang, D. Chao, X. Wang, X. Zhang, S. Chen, B.K. Tay, H. Huang, H. Zhang, W. Mai, H.J. Fan, All metal nitrides solid-state asymmetric supercapacitors, *Adv. Mater.* 27 (2015) 4566–4571.
- [55] P. Yang, D. Chao, C. Zhu, X. Xia, Y. Zhang, X. Wang, P. Sun, B.K. Tay, Z.X. Shen, W. Mai, H.J. Fan, Ultrafast-charging supercapacitors based on corn-like titanium nitride nanostructures, *Adv. Sci. J.* 3 (2015) 1500299.
- [56] M. Yu, Y. Han, X. Cheng, L. Hu, Y. Zeng, M. Chen, F. Cheng, X. Lu, Y. Tong, Holey tungsten oxynitride nanowires: novel anodes efficiently integrate microbial chemical energy conversion and electrochemical energy storage, *Adv. Mater.* 27 (2015) 3085–3091.
- [57] B. Yao, M. Li, J. Zhang, L. Zhang, Y. Song, W. Xiao, A. Cruz, Y. Tong, Y. Li, TiN paper for ultrafast-charging supercapacitors, *Nano-Micro Lett.* 12 (2019) 3.
- [58] C. Zhu, Y. Sun, D. Chao, X. Wang, P. Yang, X. Zhang, H. Huang, H. Zhang, H.J. Fan, A 2.0 V capacitive device derived from shape-preserved metal nitride nanorods, *Nano Energy* 26 (2016) 1–6.
- [59] J.A. Mejías, S. Lago, Calculation of the absolute hydration enthalpy and free energy of H⁺ and OH, *J. Chem. Phys.* 113 (2000) 7306–7316.
- [60] A. Bankura, A. Chandra, A first principles theoretical study of the hydration structure and dynamics of an excess proton in water clusters of varying size and temperature, *Chem. Phys.* 387 (2011) 92–102.
- [61] J. Chmiola, G. Yushin, Y. Gogotsi, C. Portet, P. Simon, P.L. Taberna, Anomalous increase in carbon capacitance at pore sizes less than 1 nanometer, *Science* 313 (2006) 1760–1763.
- [62] C. Largeot, C. Portet, J. Chmiola, P.-L. Taberna, Y. Gogotsi, P. Simon, Relation between the ion size and pore size for an electric double-layer capacitor, *J. Am. Chem. Soc.* 130 (2008) 2730–2731.
- [63] L. Degrève, S.M. Vichi, C.Q. Junior, The hydration structure of the Na⁺ and K⁺ ions and the selectivity of their ionic channels, *Biochim. Biophys. Acta* 1274 (1996) 149–156.
- [64] Q. Mahmood, S.K. Park, K.D. Kwon, S.-J. Chang, J.-Y. Hong, G. Shen, Y.M. Jung, T. J. Park, S.W. Khang, W.S. Kim, J. Kong, H.S. Park, Transition from diffusion-controlled intercalation into extrinsically pseudocapacitive charge storage of MoS₂by nanoscale heterostructuring, *Adv. Energy Mater.* 6 (2016) 1501115.
- [65] J. Wang, J. Polleux, J. Lim, B. Dunn, Pseudocapacitive contributions to electrochemical energy storage in TiO₂ (anatase) nanoparticles, *J. Phys. Chem. C* 111 (2007) 14925–14931.
- [66] J. Zhou, Q. Kang, S. Xu, X. Li, C. Liu, L. Ni, N. Chen, C. Lu, X. Wang, L. Peng, X. Guo, W. Ding, W. Hou, Ultrahigh rate capability of 1D/2D polyaniline/titanium carbide (MXene) nanohybrid for advanced asymmetric supercapacitors, *Nano Res.* 15 (2021) 285–295.
- [67] R.S. Nicholson, Theory and application of cyclic voltammetry for measurement of electrode reaction kinetics, *Anal. Chem.* 37 (1965) 1351–1355.
- [68] A.J. Bard, L.R. Faulkner, *Electrochemical Methods: Fundamentals and Applications*, second ed., Wiley, New York, 2001.
- [69] B. Babu, M.M. Shajumon, Understanding how degree of crystallinity affects electrochemical kinetics of sodium-ion in Brown TiO₂ nanotubes, *Chemelectrochem* 8 (2021) 2180–2185.
- [70] Y. Shen, J.R. Eltzholz, B.B. Iversen, Controlling size, crystallinity, and electrochemical performance of Li₄Ti₅O₁₂ nanocrystals, *Chem. Mater.* 25 (2013) 5023–5030.
- [71] D. Marx, M.E. Tuckerman, J. Hutter, M. Parrinello, The nature of the hydrated excess proton in water, *Nature* 397 (1999) 601–604.
- [72] C. Yan, H.-R. Li, X. Chen, X.-Q. Zhang, X.-B. Cheng, R. Xu, J.-Q. Huang, Q. Zhang, Regulating the inner Helmholtz plane for stable solid electrolyte interphase on lithium metal anodes, *J. Am. Chem. Soc.* 141 (2019) 9422–9429.
- [73] J. Liu, J. Wang, Y. Ni, J. Liu, Y. Zhang, Y. Lu, Z. Yan, K. Zhang, Q. Zhao, F. Cheng, J. Chen, Tuning interphase chemistry to stabilize high-voltage LiCoO₂Cathode material via spinel coating, *Angew. Chem. Int. Ed.* 61 (2022) e202207000.
- [74] Z. Guo, T. Wang, H. Wei, Y. Long, C. Yang, D. Wang, J. Lang, K. Huang, N. Hussain, C. Song, B. Guan, B. Ge, Q. Zhang, H. Wu, Ice as solid electrolyte to conduct various kinds of ions, *Angew. Chem. Int. Ed.* 58 (2019) 12569–12573.
- [75] L. Yan, J. Huang, Z. Guo, X. Dong, Z. Wang, Y. Wang, Solid-state proton battery operated at ultralow temperature, *ACS Energy Lett.* 5 (2020) 685–691.
- [76] S. Lin, J. Tang, K. Zhang, T.S. Suzuki, Q. Wei, M. Mukaida, Y. Zhang, H. Mamiya, X. Yu, L.-C. Qin, High-rate supercapacitor using magnetically aligned graphene, *J. Power Sources* 482 (2021) 228995.
- [77] M.F. El-Kady, V. Strong, S. Dubin, R.B. Kaner, Laser scribing of high performance and flexible graphene-based electrochemical capacitors, *Science* 335 (2012) 1326–1330.
- [78] Z. Li, Y. Zhu, F. Zhang, K. Zhou, H. Jiang, L. Liu, L. Gai, Wide-temperature activated carbon-based symmetric supercapacitors with impressive performance empowered by H3PO4 electrolyte, *J. Power Sources* 584 (2023) 233629.